Nanoscale

PAPER
Irle *et al.*
High-temperature transformation of Fe-decorated single-wall carbon nanohorns to nanooysters: a combined experimental and theoretical study

NCNST

RSCPublishing

Nanoscale

PAPER

High-temperature transformation of Fe-decorated single-wall carbon nanohorns to nanooysters: a combined experimental and theoretical study†

K. R. S. Chandrakumar,[a] Jason D. Readle,[c] Chris Rouleau,[c] Alex Puretzky,[c] David B. Geohegan,*[c] Karren More,[c] Veena Krishnan,[d] Mengkun Tian,[d] Gerd Duscher,[cd] Bobby Sumpter,[c] Stephan Irle*[b] and Keiji Morokuma*[a]

The processes by which single-wall carbon nanohorns are transformed by iron nanoparticles at high temperatures to form "nanooysters", hollow graphene capsules containing metal particles that resemble pearls in an oyster shell, are examined both experimentally and theoretically. Quantum chemical molecular dynamics (QM/MD) simulations based on the density-functional tight-binding (DFTB) method were performed to investigate their growth mechanism. The simulations suggest that the nanoparticles self-encapsulate to form single-wall nanooysters (SWNOs) by assisting the assembly of dangling carbon bonds, accompanied by migration of the metal particle inside the carbon structure. These calculations indicate that the structure of the oyster consists primarily of hexagons along with a few pentagons that are predominantly formed near the former nanohorn edges as a result of their fusion. Experimental observations of large diameter nanoparticles inside multiwall carbon shells indicate that migration and coalescence of many iron particles must occur, perhaps by the convergence of smaller SWNOs or carbon-coated Fe-nanoparticles, whereby the void space is generated by the corresponding increase in the carbon shell surface area to metal nanoparticle volume.

Introduction

In the last few decades, both experimental and theoretical research groups have made remarkable contributions to the synthesis of different forms of carbon based nanomaterials including carbon fullerenes,[1,2] nanotubes,[1,3–6] graphenes,[6–8] nanocones,[9–15] nanohorns,[16–24] metallofullerenes,[25,26] and nanoscrolls.[27] Here, we report a new member to this class of materials, so-called "nanooysters" which are encapsulated metal nanoparticles within otherwise hollow single-wall or multiwall carbon shells. The nanooysters are produced by the condensed phase conversion of carbon nanohorns and small graphene fragments that were first produced by laser vaporization of pure carbon targets, then surface-decorated with iron nanoparticles at room temperature, and then exposed to rapid, high-temperature annealing.

[a]Fukui Institute of Fundamental Chemistry, Kyoto University, Kyoto 606-8103, Japan. E-mail: keiji.morokuma@emory.edu

[b]Institute for Advanced Research and Department of Chemistry, Nagoya University, Nagoya 464-8602, Japan. E-mail: sirle@chem.nagoya-u.ac.jp

[c]Oak Ridge National Laboratory, Oak Ridge, TN, USA. E-mail: geohegandb@ornl.gov

[d]University of Tennessee, Knoxville, TN, USA

† Electronic supplementary information (ESI) available: Final structures of trajectories A–J at 1500 K and 2500 K. See DOI: 10.1039/c2nr31788e

The motivation for these experiments was our discovery from *in situ* diagnostic experiments that single-wall carbon nanotubes (SWNTs) grow at high rates (up to 1 micron per second) in laser vaporization plumes by the conversion of condensed carbon (fullerenes, graphene flakes, superfullerenes) and metals.[28] After co-ablation of a target containing 98% C and 2% Ni/Co into Ar gas at 1200 °C the carbon in the plume was found to condense first ($\sim$200 μs after laser ablation), followed by condensation of the metal ($t \sim$ 1 ms).[29] We concluded that efficient nucleation and growth of SWNTs therefore arises from metal-decorated carbon clusters at high temperature in the plume. Interestingly, without the metal catalyst and with extended lifetime of the hot laser plasma, carbon self-assembles very efficiently into single-wall carbon nanohorns (SWNHs) at similar growth rates by laser vaporization.[10,11,16,17] Condensed phase carbon therefore appears to be the feedstock, which can assemble either without a catalyst into SWNHs, or be decomposed in the presence of a catalyst into SWNTs.[28,30,31,53] The catalyst-assisted decomposition and reassembly of condensed phase carbon into long SWNTs by catalyst nanoparticles has been demonstrated, both in terms of regrowth from pre-nucleated SWNT seeds and non-nanotube carbon, at temperatures between 900 and 1600 °C,[28] and SWNT precursor formation was observed at temperatures as low as 600 °C.[31] Interestingly, only large 2–20 nm nanoparticles are found after seconds of annealing time at high temperature, despite the

narrow 1.2–1.4 nm diameter distribution of SWNTs produced. Consequently, aggregation of metal nanoparticles seems to occur during the condensed phase conversion process.

To understand the condensed phase nucleation and growth of carbon nanostructures by metal clusters, single-wall carbon nanohorns produced by laser vaporization of pure carbon were chosen as a feedstock. Nanohorns are similar to nanocones, which are capped with a single five-membered ring,[12–15] but are more tube-like with several pentagons in their apex region.[16–20] Nanohorns are almost always found in the form of spherical aggregates due to van der Waals interaction, and the wall-to-wall distance between adjacent nanohorns is ∼0.4 nm. These nanohorn aggregates are commonly referred to as dahlias or buds because of the flower-like resemblance displayed by the large number of short, horn-shaped tubules that stick out in all directions.[11,16] One of the most interesting properties of these SWNHs is the enhanced localized electron density in the vicinity of the pentagonal rings.[12–15,18–20] Charlier and Rignanese have shown the correlation between the electronic structure and the conical atomic structure, and attributed the existence of a prominent sharp density of states to the presence and the relative topology of the pentagons at the apex of the cones.[12]

During growth, the length of the nanohorn is shown to increase at ∼1 nm per ms of growth time, indicating that SWNHs can self-assemble at rates similar to those found in metal catalyst-assisted synthesis (e.g., μm s^{-1} "supergrowth").[28] However, despite theoretical attempts to simulate their growth[33] the process by which SWNHs self-assemble remains a mystery.[32] Fig. 1 may provide clues, though, and shows an atomic-resolution micrograph of as-synthesized SWNHs having many loose patches of small graphene flakes adhering to their sidewalls, indicating that the self-assembly of nanohorns, and possibly that of SWNTs, may proceed via graphene flakes that are driven by energy considerations to satisfy the dangling bonds at their edges. If defects such as pentagons and vacancies/holes are incorporated during this rolling-up of graphene flakes, nanocones should be formed as a first step in the formation of

nanohorns. If small metal catalyst nanoparticles are present during this process then single wall carbon nanotubes are the likely outcome.

Here, we experimentally and theoretically investigate the condensed phase conversion process of graphitic, single-wall carbon nanostructures by metal clusters. In the experiments, pre-formed SWNHs, which include small graphene flakes and other byproducts produced in the laser vaporization plume (see Fig. 1), are used as the carbon feedstock material for conversion by 2–3 nm Fe nanoparticles, which are deposited by electron beam evaporation in a separate step prior to rapid thermal annealing. These decorated SWNHs are a perfect system to explore the condensed phase conversion mechanism because their rough morphology – full of protruding nanocones – serves to lodge metal nanoparticles, thereby restricting diffusion. SWNHs possess a variety of interesting defect sites but appear to be entirely single-wall carbon nanostructures on their outer perimeters (although their internal bonding may contain sp^3 carbon bonds). Therefore, they are suitable as highly interesting test materials for understanding the conversion of single-wall carbon (in graphene flakes, nanocones, or nanohorns) into closed nanostructures, where it is assumed that the metal nanoparticles will partially dissolve or reconstruct the defective single-wall carbon nanostructures.

Since the deposited nanoparticles are typically observed to contact the top portions of two or more existing carbon nanohorns in the nanohorn aggregates, theoretical investigations need to take into account the metal decoration of two or more nanohorns. A recent simulation was devoted to the Ni-assisted transformation of graphene flakes to fullerenes, using a semi-classical reactive force field.[34] In most cases, the graphene flakes separated from the nickel particles, and only large nickel clusters remained attached to become encapsulated within the shells. However, effects of charge transfer and the change in the electronic structure of the graphene flakes upon restructuring could not be taken into account due to the classic approach employed. In the present study, such aggregates are modeled using first principles density functional theory (DFT) and are subjected to high-temperatures using direct quantum chemical molecular dynamics (QM/MD) simulations based on the self-consistent-charge density-functional tight-binding (DFTB) approach. Although it is obvious that experimental timescales of μs or ms cannot be achieved in such simulations, we were able to perform MD simulations on the 100 ps time scale, which still provides insight into the key processes of the transformation from two isolated carbon nanohorns, joined by a single iron nanoparticle into a nanooyster. Single-wall nanooysters (SWNOs) can be regarded as gigantic metallofullerenes, which are essentially metal quantum dots, protected from chemical modifications by their carbon shells.

Methods

Synthesis of single-wall carbon nanohorns

Laser ablation synthesis of long single wall carbon nanohorns was performed in a high temperature reactor described in ref. 32. In brief, an industrial grade, variable pulse width Nd:YAG laser
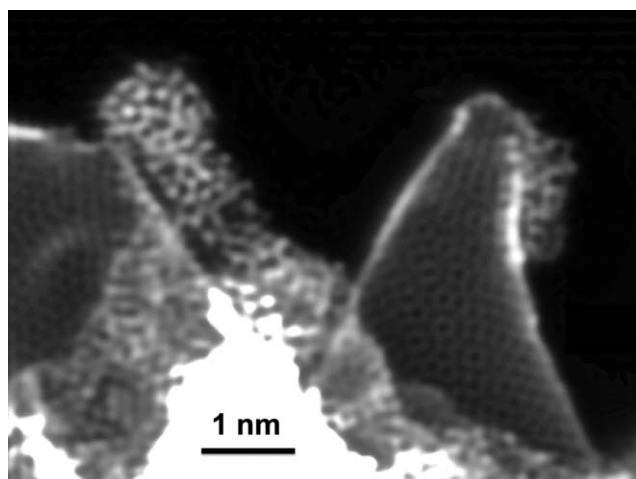

Fig. 1 Aberration-corrected, atomic resolution, Z-STEM image of SWNHs and unconverted, graphene flakes. Scale bar is 1 nm.

(600 W maximum average power, 0.5–50 ms pulse width, 1–500 Hz repetition rate) was used to vaporize a graphite target placed in a fused quartz tube (3″ diameter, 48″ length) in flowing Ar at 1100 °C. The target (1″ diameter, 1.4 g cm^{-3} density) was fabricated using graphite cement (Dylon), and was mounted on a graphite holder in the center of the fused quartz tube within a hinged furnace (Lindberg Blue, maximum temperature 1200 °C). The entire system was evacuated using a mechanical pump and flowing Ar (99.999% at 4300 sccm) was used as a background gas to confine the ablation plume and carry the nanomaterials out of the furnace into a collection chamber fitted with a HEPA filter. The laser beam (20 ms pulse width, 91 J per pulse, and 5 Hz repetition rate) was delivered through 0.6 mm diameter fiber optic cable, and focused by collimating (f = 200 mm) and focusing (f = 1000 mm) lenses through a window to a 3 mm diameter circular spot on the target. These lenses were mounted on a robotic arm, and were moved to scan the laser beam across the target in a predesigned raster pattern to achieve uniform erosion during the ablation process.

Fe-decoration and annealing of nanohorns to form nanooysters

Approximately 3 mg of material from the collection chamber were dispersed in 1 ml of *N*,*N*-DMF by sonication for 10 minutes, and then spun onto a Si wafer at 3000 rpm for 1 minute. The wafer was then decorated with a nominal 2 nm layer of Fe by electron beam evaporation, and a sample of this material was transferred to a Mo TEM grid by first wetting the Si wafer with methanol, and then dragging the grid through the resultant slurry. After allowing the grid to dry, it was then placed at the bottom of a small, 6 mm long × 3 mm diameter, graphite crucible for rapid thermal processing in a custom laser-processing chamber using the laser described above and a separate fiber-coupled lens delivery system. The crucible was capped with a loosely fitting graphite lid which permitted evacuation of the crucible but prevented direct exposure of the grid to the laser beam. After evacuating the chamber to less than 10 mTorr, a flowing 200 sccm/30 sccm Ar–H$_2$ mixture at 1.8 Torr was introduced. The crucible lid was typically laser irradiated (3.5 mm diameter laser spot, 0.37 J per pulse, 0.5 ms pulse width, 150 Hz) for less than 2 minutes. A two-color pyrometer (2 ms resolution) was used to measure the heating rate of the crucible lid, which achieved 1300 °C within 30 seconds, and 2225 °C within 45 seconds. Video imaging of the heating of the lid and the crucible body was performed through another port in the chamber. The color temperatures of the various points on the crucible could be linked to the pyrometer measurements in this way. Laser irradiation was maintained for a sufficient time (<35 seconds) to ensure that the bottom of the crucible achieved 1000 °C and maintained this temperature for 10 seconds during the heating cycle. Once the beam was shuttered, the crucible cooled to 500 °C in approximately 45 seconds.

Computational details and models

The density-functional tight-binding (DFTB) method is a computationally cost effective and accurate method that has been used by us previously for direct QM/MD simulations. In the present study, we employed the self-consistent-charge DFTB (SCC-DFTB) method[35,36] together with the transition metal–carbon parameters[37] developed by our group. Using this approach, the growth of a seed single-wall nanotube attached to a Fe$_{38}$ nanoparticle[38] and cap nucleation on iron and nickel nanoparticles[39] was successfully simulated. The detailed computational methodology employed in this work has been described in detail elsewhere.[40] The SCC-DFTB method is applied in combination with a finite electronic temperature approach with T_e = 10 000 K to evaluate the quantum chemical Mermin free energy on the fly.[41,42] The equations of motion for all MD simulations were integrated using the velocity-Verlet integrator with a time step of 1 fs, and the nuclear temperature was controlled at constant temperature in the NVT ensemble by connecting the Nose–Hoover chain thermostat to the degrees of freedom of the present model system.[43]

As a model system for these studies, we choose a Fe$_{38}$ metal cluster (a truncated octahedron fcc-Fe$_{38}$ magic cluster) as the catalyst, and a SWNH with a well-defined length that had one pentagon at its center – see Fig. 7. The disclination angle of the SWNH is 60° and its diameter is roughly ∼1.3 nm. We initially optimized the SWNH–Fe$_{38}$ structure before it was equilibrated with different initial velocities for 10 ps. The process was repeated for 20 different trajectories, split equally between the temperatures of 1500 K and 2500 K. Finally, each of the trajectories were kept at their corresponding process temperature for an additional 30–40 ps. The assumption of a constant temperature canonical ensemble (NVT) is justified by the short timescale of the simulations, since experimental cooling rates occur on much larger timescales.

DFT calculations were performed using the local density (LDA) and generalized gradient (GGA) approximations as implemented in version 4.6.6 of the Vienna *ab initio* simulation package (VASP).[44] The Kohn–Sham equations were solved using the projector augmented wave (PAW) approach[45] and a plane-wave basis with a 400 eV energy cutoff. For the generalized gradient approximation, the exchange-correlation functional of Perdew, Burke, and Ernzerhof (PBE) was utilized.[46] Electronic convergence was defined as a consistency between successive cycles of less than 10^{-4} eV. Each system was placed in a cell that ensured at least 10 Å of vacuum in each Cartesian direction between the system and its reflection. *K*-point sampling was restricted to a single point, the Γ point, a choice that is common for the finite cluster calculations performed here. Spin polarized (sp) as well as unpolarized (nsp) approaches were employed in DFT calculations. The binding energies were estimated by the difference in energy for the fully optimized systems (*e.g.*, SWNH–Fe$_{38}$) and the optimized individual components (SWNH and Fe$_{38}$).

Results and discussion

SWNHs were decorated with Fe-nanoparticles by first evaporating a 2 nm (nominal) Fe film by electron-beam evaporation in a vacuum. The decorated material was then transferred to a molybdenum TEM grid, which was placed inside a specially

designed graphite container, and subjected to rapid laser heat treatment in Ar/H$_2$ (see the Methods section). The goal was to subject the metal-decorated nanohorns to temperatures similar to those found typically in SWNT growth (1000–1200 °C), and for times similar to those encountered in laser vaporization plumes (*i.e.*, 10–15 seconds). This was done to investigate whether metal nanoparticles can alter well-defined, single-wall carbon nanostructures (*e.g.*, nanohorns, nanocones, graphene flakes, fullerenes) and convert them to nanotubes or other closed-shell structures. High-resolution microscopy of the annealed products was performed using a Hitachi HF-3300 bright field TEM/STEM and an aberration-corrected dedicated STEM (VG HB-501UX) with a Gatan EELS spectrometer. Fig. 2 shows typical nanohorn aggregates after deposition and dewetting of a nominal 2 nm layer of Fe prior to annealing.

Distinct Fe crystallites with typical diameters of approximately 2–3 nm were often observed to be in contact with two or more nanohorn tips. Their presence is attributed to dewetting of the deposited Fe film. Lattice fringes indicate that the particles are crystalline. Some regions on the decorated SWNHs had thicker coatings of Fe nanoparticles than others due to shadowing induced by the nanohorn aggregates during the deposition process.

Fig. 3a and b show the case when SWNOs just start to develop after heat treatment. The heat treatment changes the Fe particle size distribution from the as-deposited 2–3 nm up to 20 nm, and all of these larger particles are generally encased in one or more layers of carbon, with the smaller particles typically exhibiting either incomplete or single layers. In the cases where the particle size increases, the empty space surrounding one or more sides of
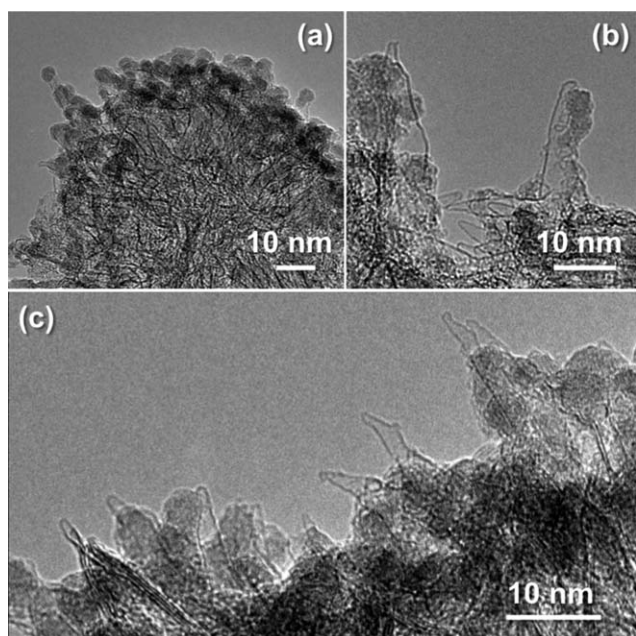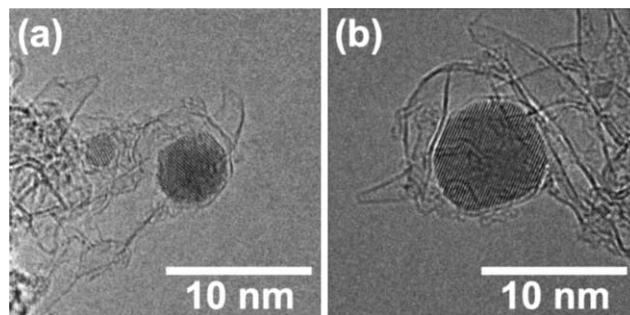
Fig. 3 HR-TEM images taken of the Fe-decorated SWNHs after laser heating. The as-deposited Fe nanoparticles were observed to grow in size to 5–20 nm, encased within single-wall (or multiwall) carbon nanostructures either tightly bound or with empty space.

the particle could often be found, as in Fig. 3b, where three of the sides of the hexagonal particle are not in apparent contact with a resulting carbon nanostructure, and the other three sides are in close proximity to a carbon edge that conforms to its shape. The variety of single-wall carbon nanostructures in contact with the metal nanoparticles are exhibited in Fig. 3b, which shows a carbon nanocone tip, folded nanohorn sidewalls, along with carbon flakes and clusters of various sizes.

As shown in Fig. 4a and b, a great variety of irregular and hollow carbon nanostructures appear to be growing by the decomposition and conversion of nanohorns and graphene flakes. In Fig. 4a, an irregular, 30 nm long, few-layer, hollow, nanotube-like structure appears to be growing from the nanoparticle that is half-embedded within the nanohorn aggregate, while nearby another few-layer capped structure has lifted off. However, several large nanoparticles appear to be encapsulated within a single layer carbon shell. In Fig. 4a and b the shells are all relatively thin (≤3 layers), and in Fig. 4b and c it appears to retain sharp faceted shapes very similar to those of the particles that are enclosed. Larger core particles such as the 15 nm diameter particle in Fig. 4c tended to be enclosed in thicker multilayer graphitic shells, which in this case varied from approximately 0.5 nm to 1.5 nm thick (corresponding to between ~4 and ~6 graphene layers). This variation further illustrates the often-asymmetric nature of the shells in which the graphitic layers are not necessarily continuous. The innermost facets of the Fe nanoparticle inside the nanooyster of Fig. 4c appear to have a single graphitic layer in direct contact with Fe.
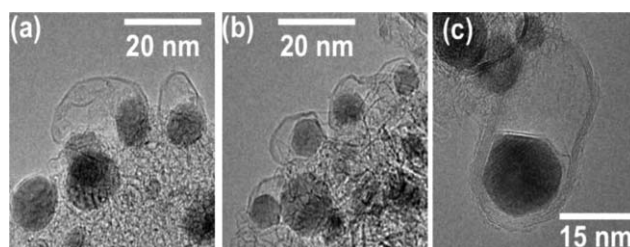

Fig. 2 HR-TEM images taken of the Fe-decorated SWNHs before laser heating. (a) SWNH aggregate ball decorated preferentially from the top with Fe nanoparticles. (b and c) Higher magnification views of SWNH tips in contact with one or more Fe nanoparticles on the periphery of the SWNH aggregate.

Fig. 4 Bright-field HR-TEM of nanooysters with complete, multilayer shells.

To determine whether or not the metal nanoparticles were completely enclosed within the carbon layers, a series of scanning electron microscopy (SEM), Z-contrast scanning transmission electron microscopy (Z-STEM), and bright field STEM images of many nanooysters were taken. Fig. 5a and b compare the bright- and dark-field STEM images, respectively, of a nanooyster with a particle diameter of ∼15 nm and a graphitic shell with >10 layers. Representatively, the large particle appears to be enclosed within the carbon shell. This conclusion is verified by the SEM image of the nanooyster presented in Fig. 5c, which shows only the carbon surface. Of course, the nanoparticles could have protruded through the other side of the carbon shell, however no such protrusions were found despite having checked tens of nanoparticles, leading to the conclusion that the metal nanoparticles were indeed encased in carbon shells. The prevalence of the nanooysters on the annealed, Fe-decorated SWNHs is shown in the lower magnification SEM image of Fig. 5d in which numerous nanooysters are observed as blisters or bubbles on the roughly spherical 50–80 nm diameter SWNH aggregates. This appearance is attributed to the volume displacement corresponding to the hollow regions of the nanooysters.

Further characterization of the nanooysters was performed using energy dispersive X-ray spectroscopy (EDS) and electron energy loss spectroscopy (EELS). Through these techniques, we made the surprising discovery that the metallic core particles varied in composition, ranging from pure Fe to pure Mo. The unexpected presence of Mo is attributed to the incorporation of loose fragments from the Mo grid on which laser processing was performed. However, no obvious effect of the core particle composition on the nanooyster characteristics was observed,
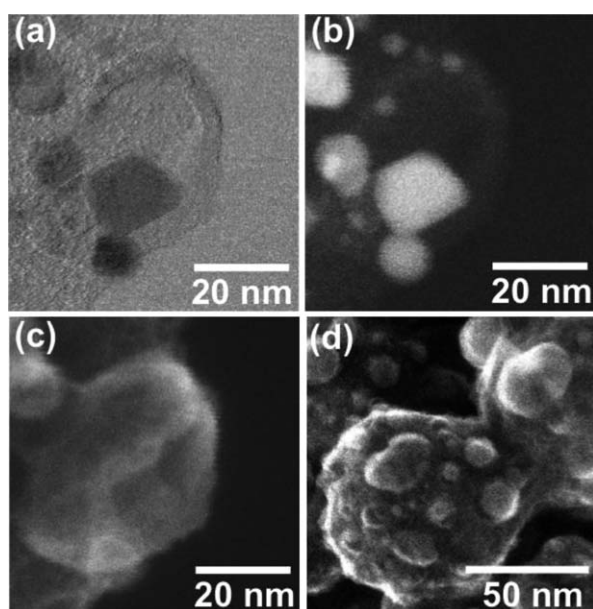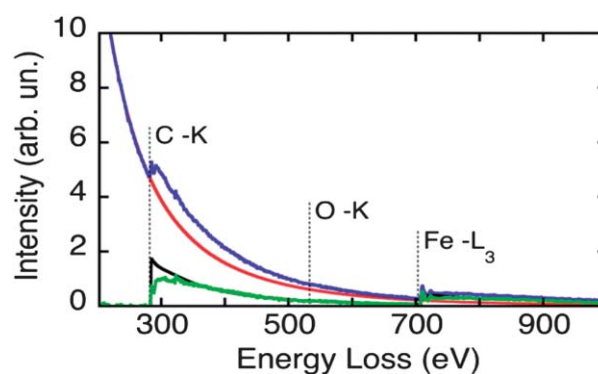
implying that the growth mechanism described here may be shared by a variety of metal–carbon combinations. The EELS spectrum of a typical Fe particle is shown in Fig. 6. The spectrum has an energy resolution of about 0.3 eV and clearly shows the C–K ionization edge at 284 eV and the Fe–L_3 edge at 708 eV. Analysis of the EELS edge-onsets corresponding to the metallic core particles indicated that, regardless of size or composition, none of them were carbides. This suggests that any carbon which may have been dissolved into the metal during growth was precipitated back out as the sample cooled. A model fit with these two edges of a modified power law background and the O–K edge revealed that no oxygen could be detected. The Fe L_3, L_2 ionization edge of the spectrum in Fig. 6 was fitted with a Hartree–Slater cross-section and two Gaussians. The result of the fit is that the L_3/L_2 white-line ratio is 4.9, which is lower than what has been found for any iron oxide,[47] again revealing Fe particles that are not oxidized. The samples were briefly exposed to ambient air during handling, so the lack of detectable oxidation indicates that the Fe nanoparticles inside the carbon nanooysters (CNOs) are encapsulated and protected. It is known that a layer of graphite or graphene can prevent corrosion of metals,[48,49] and this effect is used to produce single layers of graphene. Therefore, encapsulation of the Fe nanoparticles by CNOs and/or by conformal layers of carbon within the CNOs (as suggested by Fig. 4c) may be responsible for the observed lack of oxidation.

QM/MD simulations of the formation of nanooysters

Before an MD study of formation mechanisms can be carried out, it is important to check the validity of the potentials employed. In this case, it is necessary to take into account the effects of charge transfer, the high density of metal d-states, and carbon π-conjugation. As a result, we employ the self-consistent-charge (SCC) version of the DFTB method.[35–37] Note that SCC-DFTB (in the following briefly referred to as "DFTB") has been employed successfully as in our previous simulations of SWNT nucleation, growth, and defect healing.[38–40] As a first step towards the study of the formation of nanooysters, we consider a Fe–nanohorn complex, and compare DFTB results with those

Fig. 5 (a) Bright- and (b) dark-field STEM images of a nanooyster showing the metal nanoparticle within. (c) SEM image of the same structure shows that the metal nanoparticle is inside a carbon shell. (d) SEM image showing the prevalence of the bulbous nanooysters on the exteriors of the annealed, Fe-decorated SWNHs.

Fig. 6 EELS spectrum of an Fe particle in a nanooyster. The spectrum (blue) was fitted with a background (red) and the cross-section of the elements (black). The background subtracted spectrum is shown in green for comparison. The model fit reveals that there is no oxygen in the analyzed area.

from the DFT method. In previous studies, DFTB results for the geometry and binding energy details, especially for carbon clusters and nanotubes, and their interaction with transition metals, have been shown to be comparable with conventional DFT findings.[40] Although DFTB results for the case of nanohorns and their interaction with an iron nanoparticle are also expected to be in good agreement with DFT results, we have calibrated our geometrical and binding energy values obtained by the SCC-DFTB method with those from DFT methods. The results are summarized in Table 1 and demonstrate that, as expected, the DFTB approach adequately captures the geometry and the binding energies that are associated with the interfaces between the carbon conical structures and the Fe_{38} nanoparticle. Binding energies for the SWNH–Fe_{38} are underestimated compared to DFT/LDA and DFT/GGA calculations as reflected in the longer metal–carbon bond lengths.

Beginning with the initial geometry as shown in Fig. 7, ten different trajectory replicas at 1500 K and 2500 K were generated using different initial velocities, and they are labeled with Roman letters A–J for each temperature. Note that all trajectories were run for 50–70 ps. The particular choice to place the metal particle on the tip of the SWNHs was motivated by the fact that the experimental samples were prepared using surface-decorated SWNH aggregates, where the SWNH tips are believed to point away from the aggregate cores. Snapshots of the oyster formation at 2500 K are shown in Fig. 8 for trajectory I. It is evident from this sequence that there are three fundamental steps that occur before the shell-like structure is formed: (i) initially, both the SWNHs flip from the tip position to the edge at the catalyst interaction site, (ii) the SWNHs move to the top of the catalyst and the nanohorns start interacting with each other, and (iii) cage closure leading to the formation of the nanooyster structure. Step (i), the rapid initial flip of the SWNH structure, is a general feature that is observed in all the trajectories within 3 to 4 ps. The process of zipping of the two SWNHs together occurs very quickly and is accompanied by the formation of several new pentagonal and hexagonal rings within the following 3 to 5 ps. The temperature plays an important role for these processes as evidenced by degradation of the oysters above 2500 K. As may be expected, the simulations indicate that the nanooyster formation occurs more rapidly at 2500 K than at 1500 K. In both cases, this process is driven by
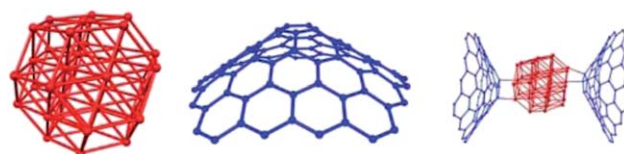

Fig. 7 Initial geometry of the Fe_{38} cluster, SWNH and metal–SWNH complex employed in QM/MD Simulations.

the saturation of the open edges of the SWNHs. It is also important to note that, for the formation of nanooysters to be favored, the SWNH edge–edge interaction must be stronger than the SWNH–catalyst interaction.

The structures obtained from all the trajectories at 1500 K and 2500 K are shown in Fig. S1 and S2 in the ESI.† These results
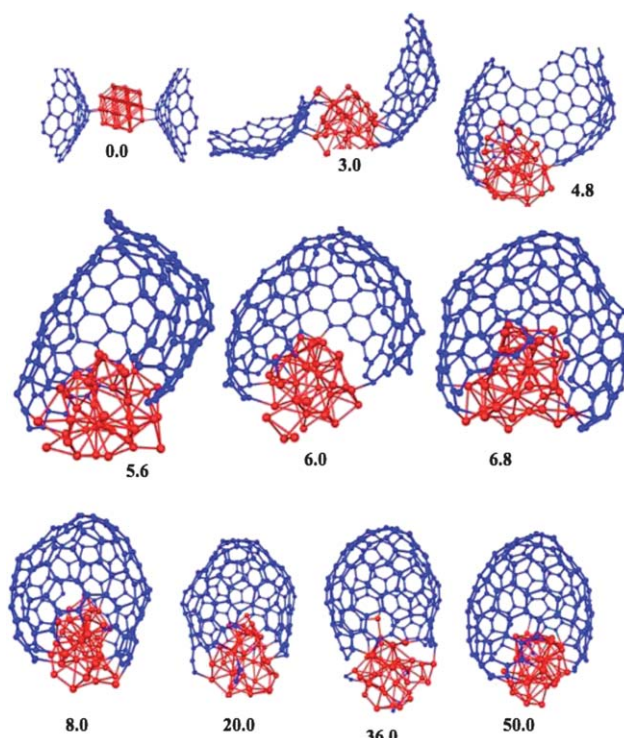

Fig. 8 Snapshots of the nanooyster growth at 2500 K showing key steps in the process. Time is indicated in picoseconds.

Table 1 DFTB and DFT results of the interaction energy ΔE and geometrical parameters of the nanohorn interacting with iron nanoclusters, Fe_{38}

System	DFTB			DFT		
	M–C[a]	C–C[b]	ΔE[c]	M–C	C–C	BE[d,e]
SWNH–Fe_{38}	2.275	1.434/1.497	−2.16	1.944(sp/LDA)	1.447/1.487(sp/LDA)	−3.36(sp/LDA)
				1.944(nsp/LDA)	1.435/1.487(nsp/LDA)	−3.92(nsp/LDA)
				1.975(nsp/GGA)	1.452/1.495(nsp/GGA)	−2.45(nsp/GGA)
SWNH–Fe_{38}–SWNH[f]	2.281	1.434/1.498	−3.91	2.489(nsp/LDA)	1.414/1.450(nsp/LDA)	−5.97(nsp/LDA)
				1.910(nsp/GGA)	1.432/1.461(nsp/GGA)	−3.42(nsp/GGA)

[a] M–C: the shortest distance between Fe_{38}–carbon@SWNH pentagon (Å). [b] C–C: the shortest/longest distance between carbon–carbon at the SWNH pentagon (Å). [c] ΔE: interaction energy in eV. [d] DFT using LDA and GGA with spin polarization (sp) and without (nsp). [e] The plane-wave energy cutoff for the isolated iron nanoparticle was taken as the value set in the pseudopotential, 267.9 eV. [f] Interaction energy is listed for removing one SWNH (e.g., $2 \times \Delta E$ is the total energy to separate two SWNHs and a nanoparticle).
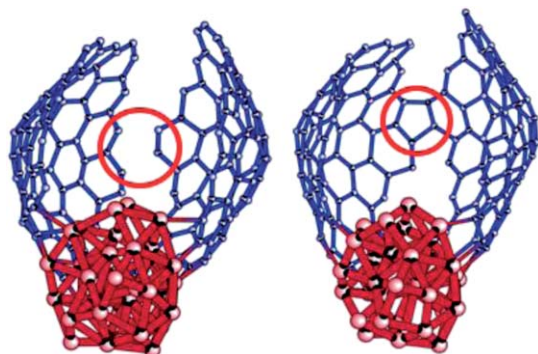
Fig. 9 Mechanism of edge coalescence leading to partial (open) nanooyster formation.

reveal that, for a given temperature, two different types of structures are typically observed after the interaction of two nanohorns with each other in the presence of an iron catalyst. At 2500 K these structures fall into two groups: metal cluster encapsulated horns on the one hand, and incomplete encapsulation on the other where only one horn covers the metal particle, and the only attached at a single edge. At 1500 K, incomplete encapsulation is found more often than at the higher temperature.

During the structural transformation of the nanohorns into a nanooyster, many new pentagonal and hexagonal rings are formed when the edges of two SWNHs merge to form a continuous sp^2 carbon network. Fig. 9, for example, shows the formation of a pentagon. Pentagons are formed when one of the five armchair corners of the nanohorn edges reacts with the more numerous zigzag edges of the second cone. We rarely observe that hexagons within the SWNHs transform to pentagons or heptagons *via* Stone Wales rearrangements, a process that is associated with high barriers and therefore difficult to observe in MD simulations on the present timescales. Furthermore, in contrast to the simulations by Lebedeva *et al.*,[34] we did not find dissolution of the carbon nanohorns into the metal nanoparticles. The difficulty of carbon dissolution is consistent with our previous findings of carbon nanotube growth on iron nanoparticles,[40] where we had found rapid precipitation of carbon from nickel and iron carbide nanoparticles. Our simulations reflect the experimentally documented fact that, when compared to bulk, carbon dissolution is reduced in smaller iron particles.[50]

Nature of the oyster structure

In general, the nanohorns are made up of hexagons except at the apex regions wherein pentagons are normally present. The number of pentagons are dependent on the nature of the SWNHs, and in the present case, each nanohorn has one pentagon at the apex, which is not sufficient to form the highly curved oyster structure. As discussed previously, the nanooyster structure is comprised of numerous pentagons, particularly at the edges where the two SWNHs are joined together. Our analysis shows that during the transformation, the number of

pentagons is increased to 8–10, along with additional hexagons. This ring arrangement results in the curvature, which eventually leads to the formation of a nanooyster.

It should be noted that the nanooysters are not conventional metallo-fullerenes. In metallo-fullerenes, the pentagons are uniformly distributed along with the hexagons and only a few metal atoms are normally observed inside the fullerene cage. This is in contrast to the nanooysters of our simulations, where the pentagons and hexagons are arranged alternatively at the interfacial region where the nanohorns interact with each other. The number of metal atoms attached to the oyster varies with the size of the metal nanoclusters and processing temperature. Because the iron cluster is well isolated by the carbon cage, it is believed that its magnetic properties are preserved. As a result, it may be possible to create well-aligned configurations of such structures for applications such as spin-dependent electron transport phenomena in solid-state devices.

Conclusions

The condensed phase conversion of single-layer carbon nanostructures by metal nanoparticles at high-temperatures has been studied experimentally and theoretically for the growth of "nanooysters" from Fe-decorated SWNHs. Computational simulations identified a specific pathway for the transformation of two carbon nanohorns and a Fe nanoparticle into an enclosed nanooyster, and determined two important steps in the process: (1) flipping of the SWNHs from its apex to peripheral carbon atoms at the iron catalyst site and (2) SWNH–SWNH edge interactions overcoming the SWNH–catalyst interaction, leading to catalyst encapsulation. Simulations indicate that the final structure has between eight to ten pentagons that result in a large curvature of the carbon shell and iron nanoparticles attached only at one end, consistent with the experimental observations.

In addition, the experiments confirm the presence of multiwall nanooysters, which contain much larger metal nanoparticles than those that existed before high-temperature annealing. The shapes of the encapsulated metal nanoparticles indicate that migration of the metal to form much larger nanoparticles is a key component in the formation of the nanooysters. One distinguishing feature of the nanooysters is the empty volume within the shells. This empty volume could be explained by the reduction in the surface area of carbon-coated metal nanoparticles upon consolidation. According to the QM/MD simulations, the metal clusters within the SWNOs can penetrate the oyster walls. It is therefore conceivable that two metal nanoparticles, upon contact, could merge into a single nanoparticle, with the shells of the carbon oysters rearranging to accommodate a new, larger particle. From the HRTEM images, taking into account the number of carbon shells and the size of the metal nanoparticles within the nanooyster, the combined surface area of the carbon in the multiple walls of the nanooyster is very nearly that expected from a single-layer coating of the initial 2–3 nm nanoparticles that comprise the metal nanoparticle in the nanooyster

(see Fig. 3). Combined dewetting and carbon precipitation of the metal nanoparticle from the inner walls of the nanooyster may be responsible for the observed faceted internal shapes.

This interpretation has been complemented by QM/MD modeling to demonstrate one possible mechanism by which metal nanoparticles can enable the condensed phase conversion of single-layer carbon nanostructures into enclosed shell-like nanooysters. For the small clusters in the simulation, the solubility of the metal is insufficient to digest a sizable fraction of the carbon. Nevertheless, the metal nanoparticles are nearly exposed. Therefore, it is possible that single-wall nanooysters with larger nanoparticles form by convergence of smaller nanooysters where dewetting of the metal particles from the carbon shells results in an increased surface area and associated empty space inside the nanooyster.

After the nanoparticle becomes enclosed within two or more layers, this mechanism appears less likely than the dissolution–precipitation mechanism observed by Helveg, et al.,[51] for example, wherein closed multiwall structures are observed to retain evidence of the shape of the metal nanoparticle before and after the expulsion of carbon. In this case, however, the metal nanoparticle would still need to be exposed at high temperature in order to continue to digest graphene sheet, nanocone, and nanohorn feedstock. This suggests that the final multiwall shell would need to be precipitated upon cooling, which is feasible for very large nanoparticles, but not for small nanoparticles.[50]

Clearly, both surface-reconstruction and dissolution precipitation models remain plausible for small and large nanooysters, respectively. The simulations of our experiment may also help to explain the recent experimental observations of Hunley et al.,[52] where nanotubes were apparently formed by condensed phase conversion of graphene.

Acknowledgements

References

1 M. S. Dresselhaus, G. Dresselhaus and P. C. Eklund, *Science of Fullerenes and Carbon Nanotubes*, Academic Press, New York, 1996.

2 A. Rodriguez-Fortea, A. L. Balch and J. M. Poblet, *Chem. Soc. Rev.*, 2011, **40**, 3551–3563.

3 R. Saito, G. Dresselhaus and M. S. Dresselhaus, *Physical Properties of Carbon Nanotubes*, Imperial College Press, London, 1998.

4 S. S. Wong, E. Joselevich, A. T. Woolley, C. L. Cheung and C. M. Lieber, *Nature*, 1998, **394**, 52–55.

5 M. Endo, T. Hayashi, Y. A. Kim, M. Terrones and M. S. Dresselhaus, *Philos. Trans. R. Soc., A*, 2004, **362**, 2223–2238.

6 W. R. Yang, K. R. Ratinac, S. P. Ringer, P. Thordarson, J. J. Gooding and F. Braet, *Angew. Chem., Int. Ed.*, 2010, **49**, 2114–2138.

7 M. J. Allen, V. C. Tung and R. B. Kaner, *Chem. Rev.*, 2010, **110**, 132–145.

8 X. T. Jia, J. Campos-Delgado, M. Terrones, V. Meunier and M. S. Dresselhaus, *Nanoscale*, 2011, **3**, 86–95.

9 M. H. Ge and K. Sattler, *Chem. Phys. Lett.*, 1994, **220**, 192–196.

10 A. Krishnan, E. Dujardin, M. M. J. Treacy, J. Hugdahl, S. Lynum and T. W. Ebbesen, *Nature*, 1997, **388**, 451–454.

11 M. Yudasaka, S. Iijima and V. H. Crespi, *Top. Appl. Phys.*, 2008, **111**, 605–629.

12 J. C. Charlier and G. M. Rignanese, *Phys. Rev. Lett.*, 2001, **86**, 5970–5973.

13 S. Compernolle, B. Kiran, L. F. Chibotaru, M. T. Nguyen and A. Ceulemans, *J. Chem. Phys.*, 2004, **121**, 2326–2336.

14 M. Munoz-Navia, J. Dorantes-Davila, M. Terrones and H. Terrones, *Phys. Rev. B: Condens. Matter Mater. Phys.*, 2005, **72**, 235403.

15 J. Han and R. Jaffe, *J. Chem. Phys.*, 1998, **108**, 2817–2823.

16 S. Iijima, M. Yudasaka, R. Yamada, S. Bandow, K. Suenaga, F. Kokai and K. Takahashi, *Chem. Phys. Lett.*, 1999, **309**, 165–170.

17 D. Kasuya, M. Yudasaka, K. Takahashi, F. Kokai and S. Iijima, *J. Phys. Chem. B*, 2002, **106**, 4947–4951.

18 S. Garaj, L. Thien-Nga, R. Gaal, L. Forro, K. Takahashi, F. Kokai, M. Yudasaka and S. Iijima, *Phys. Rev. B: Condens. Matter Mater. Phys.*, 2000, **62**, 17115–17119.

19 S. Bandow, A. M. Rao, G. U. Sumanasekera, P. C. Eklund, F. Kokai, K. Takahashi, M. Yudasaka and S. Iijima, *Appl. Phys. A*, 2000, **71**, 561–564.

20 S. Berber, Y. K. Kwon and D. Tomanek, *Phys. Rev. B: Condens. Matter Mater. Phys.*, 2000, **62**, R2291–R2294.

21 J. A. Nisha, M. Yudasaka, S. Bandow, F. Kokai, K. Takahashi and S. Iijima, *Chem. Phys. Lett.*, 2000, **328**, 381–386.

22 E. Bekyarova, K. Murata, M. Yudasaka, D. Kasuya, S. Iijima, H. Tanaka, H. Kahoh and K. Kaneko, *J. Phys. Chem. B*, 2003, **107**, 4681–4684.

23 H. Tanaka, H. Kanoh, M. Yudasaka, S. Lijima and K. Kaneko, *J. Am. Chem. Soc.*, 2005, **127**, 7511–7516.

24 K. Murata, M. Yudasaka and S. Iijima, *Carbon*, 2006, **44**, 818–820.

25 H. Shinohara, *Rep. Prog. Phys.*, 2000, **63**, 843–892.

26 A. Rodriguez-Fortea, A. L. Balch and J. M. Poblet, *Chem. Soc. Rev.*, 2011, **40**, 3551–3563.

27 G. Mpourmpakis, E. Tylianakis and G. E. Froudakis, *Nano Lett.*, 2007, **7**, 1893–1897.

28 D. B. Geohegan, H. Schittenhelm, X. Fan, S. J. Pennycook, A. A. Puretzky, M. A. Guillorn, D. A. Blom and D. C. Joy, *Appl. Phys. Lett.*, 2001, **78**, 3307–3309.

29 A. A. Puretzky, D. B. Geohegan, X. Fan and S. J. Pennycook, *Appl. Phys. A*, 2000, **70**, 153–160.

30 P. J. F. Harris, *Carbon*, 2007, **45**, 229–239.

31 R. Sen, S. Suzuki, H. Kataura and Y. Achiba, *Chem. Phys. Lett.*, 2001, **349**, 383–388.

32 A. A. Puretzky, D. J. Styers-Barnett, C. M. Rouleau, H. Hu, B. Zhao, I. N. Ivanov and D. B. Geohegan, *Appl. Phys. A*, 2008, **93**, 849–855.

33 T. Kawai, Y. Miyamoto, O. Sugino and Y. Koga, *Phys. Rev. B: Condens. Matter Mater. Phys.*, 2002, **66**, 033404.

34 I. V. Lebedeva, A. A. Knizhnik, A. M. Popov and B. V. Potapkin, *J. Phys. Chem. C*, 2012, **116**, 6572–6584.

35 D. Porezag, T. Frauenheim, T. Kohler, G. Seifert and R. Kaschner, *Phys. Rev. B: Condens. Matter Mater. Phys.*, 1995, **51**, 12947–12957.

36 M. Elstner, D. Porezag, G. Jungnickel, J. Elsner, M. Haugk, T. Frauenheim, S. Suhai and G. Seifert, *Phys. Rev. B: Condens. Matter Mater. Phys.*, 1998, **58**, 7260–7268.

37 G. S. Zheng, H. A. Witek, P. Bobadova-Parvanova, S. Irle, D. G. Musaev, R. Prabhakar and K. Morokuma, *J. Chem. Theory Comput.*, 2007, **3**, 1349–1367.

38 Y. Ohta, Y. Okamoto, S. Irle and K. Morokuma, *ACS Nano*, 2008, **2**, 1437–1444.

39 A. J. Page, H. Yamane, Y. Ohta, S. Irle and K. Morokuma, *J. Am. Chem. Soc.*, 2010, **132**, 15699–15707.

40 A. J. Page, Y. Ohta, S. Irle and K. Morokuma, *Acc. Chem. Res.*, 2010, **43**, 1375–1385.

41 A. D. Rabuck and G. E. Scuseria, *J. Chem. Phys.*, 1999, **110**, 695–700.

42 M. Weinert and J. W. Davenport, *Phys. Rev. B: Condens. Matter Mater. Phys.*, 1992, **45**, 13709–13712.

43 G. J. Martyna, M. L. Klein and M. Tuckerman, *J. Chem. Phys.*, 1992, **97**, 2635–2643.

44 G. Kresse and J. Hafner, *Phys. Rev. B: Condens. Matter Mater. Phys.*, 1993, **48**, 13115–13118.

45 P. E. Blochl, *Phys. Rev. B: Condens. Matter Mater. Phys.*, 1994, **50**, 17953–17979.

46 I. P. Perdew, K. Burke and M. Ernzerhof, *Phys. Rev. Lett.*, 1996, **77**, 3865–3868.

47 H. Kurata, N. Tanaka and L. Iron, *Microsc. Microanal. Microstruct.*, 1991, **2**, 183–190.

48 R. Schlogl, in *Handbook of Heterogeneous Catalysis*, ed. G. Ertl, H. Knozinger, F. Schuth and J. Weitkamp, Wiley-VCH, Weinheim, 2008, vol. 1, p. 357.

49 J. A. Moulijn, A. E. van Diepen and F. Kapteijn, in *Handbook of Heterogeneous Catalysis*, ed. G. Ertl, H. Knozinger, F. Schuth and J. Weitkamp, Wiley-VCH, Weinheim, 2008, vol. 4, p. 1829.

50 A. R. Harutyunyan, N. Awasthi, A. Jiang, W. Setyawan, E. Mora, T. Tokune, K. Bolton and S. Curtarolo, *Phys. Rev. Lett.*, 2008, **100**, 195502.

51 S. Helveg, C. Lopez-Cartes, J. Sehested, P. L. Hansen, B. S. Clausen, J. R. Rostrup-Nielsen, F. Abild-Pedersen and J. K. Norskov, *Nature*, 2004, **427**, 426–429.

52 D. P. Hunley, S. L. Johnson, J. K. Stieha, A. Sundararajan, A. T. Meacham, I. N. Ivanov and D. R. Strachan, *ACS Nano*, 2011, **5**, 6403–6409.

53 A. A. Puretzky, H. Schittenhelm, X. Fan, M. J. Lance, L. F. Allard Jr and D. B. Geohegan, *Phys. Rev. B: Condens. Matter Mater. Phys.*, 2002, **65**, 245425.